possibility of self-phase locking.[14] Also, since it is not necessary to phase match for an exact set of frequencies as in second-harmonic generation, the angular alignment and temperature of the crystal are far less critical.

From Eqs. (14) and (6) it is seen that a measurement of the ratio of spontaneously emitted power to incident power at a known temperature and signal wavelength yields the ratio of $d_{15}^2/b$. It is thus clear that if $d_{15}$ is desired, the dispersion constant $b$ must be determined. A number of alternatives are available. First, a relatively short crystal could be used and the aperture closed down until the minimum bandwidth is reached, where then $(\text{bandwidth})_{\min}=0.885/bL$. Alternatively, it may be shown by examining Eq. (13) that, for $\theta^2 \gtrsim 2\pi/Lg$, the bandwidth is given by the following:

$$\text{bandwidth}=(g/2\pi b)\theta^2, \qquad (16)$$

where $g$ is given by Eq. (12). This latter technique allows the measurement of $b$ at more easily measured bandwidths or by the measurement of the slope of the bandwidth-versus-$\theta^2$ curve. A third alternative is to measure the refractive indices of the crystal by conventional techniques and thus determine $b$ directly.

From the slope of Fig. 3, we obtain $P_s/P_p=0.18\times10^{-4}\theta^2$, which from Eqs. (6) and (14) yields $d_{15}^2/b=5.13\times10^{-36}$. From Fig. 5 and Eq. (16) we obtain $b=6.2\times10^{-10}$ sec/m, thus yielding $d_{15}=0.55\times10^{-22}\pm10\%$ in mks units which is in good agreement with the published value $d_{15}=0.56\times10^{-22}$.[14,15]

## ACKNOWLEDGMENT

The authors gratefully acknowledge many helpful discussions with M. K. Oshman.

PHYSICAL REVIEW VOLUME 168, NUMBER 3 15 APRIL 1968

# Atomic Arrangement in Vitreous Selenium

ROY KAPLOW, T. A. ROWE,* AND B. L. AVERBACH
*Department of Metallurgy and Materials Science, Massachusetts Institute of Technology, Cambridge, Massachusetts*
(Received 6 December 1967)

X-ray diffraction data at 25 and −196°C have been used to obtain radial distribution functions for amorphous and hexagonal selenium. The amorphous selenium exhibited strong correlation peaks at 2.34, 3.75, 5.8, 7.2, and 9.3 Å, with minor peaks at 4.3, 4.7, 5.1, 7.7, 10.0, and 10.5 Å. The first two distances are observed in both the hexagonal form, which consists of spiral chains, and the monoclinic forms, which consist of eight-membered puckered rings. The remaining major peaks do not correspond to intramolecular distances in any of the crystalline forms. Attempts were made to match the experimental amorphous distribution function with models which involved perturbations of the atom positions in the hexagonal and in the two monoclinic crystalline forms. A computer array consisting of 100 atom positions was used, and perturbations were chosen by a Monte Carlo procedure which allowed only those perturbations which improved the fit to the experimental distribution function. It was shown that relatively small rms static displacements, of the order of 0.20 Å, were sufficient to convert the monoclinic ring structures to the observed vitreous form, whereas much larger perturbations, of the order of 0.7 Å, were required to convert the hexagonal chain structure into a form which would give a suitable amorphous radial distribution function. The atomic configurations in the perturbed monoclinic structures consisted mainly of slightly distorted rings. There were a few locations where the rings had been opened sufficiently so that the atoms in the vicinity of the opening appeared to have the nearest-neighbor trigonal symmetry of the chain rather than of the eight-membered ring. The optical and Raman spectra provide strong evidence for the presence of $Se_8$ rings and a weaker indication of near-neighbor trigonal symmetry. We conclude that the structure of vitreous selenium consists mainly of slightly distorted $Se_8$ rings, along with an occasional ring which is opened sufficiently to develop a weak localized trigonal symmetry or a few greatly deformed chains.

## I. INTRODUCTION

THE atomic arrangement in amorphous selenium is not well established, in spite of several recent attempts to determine the structure. The problem is inherently more difficult than an analogous crystal-structure determination since diffraction data can be transformed no farther than a radial distribution function (RDF). An atomic model must then be postulated, including assumptions of thermal displacement and molecular configuration, and the corresponding radial distribution function calculated. The experimental RDF is frequently plagued by false detail, and conversely, the calculation of an RDF from an atomic model is not a trivial procedure when a crystal lattice is absent. There has thus been great uncertainty in the results for selenium, and it frequently appears that the methods of amorphous-structure determination are being developed along with the structure.

There are two basic atomic arrangements in crystalline selenium. The hexagonal form is stable at room temperature; the atoms in this structure are arranged in long parallel chains with the threefold spiral about the

* Present address: Fairchild Semiconductor, Palo Alto, Calif.

$C$ axis, with the three atoms in each unit of the spiral exhibiting $D_3$ molecular symmetry. The bonding between atoms in a chain is covalent, and the bonding between chains is of the van der Waals type. The $\alpha$ and $\beta$ monoclinic forms of selenium have the same molecular unit, which consists of an eight-atom puckered ring with a $D_{4d}$ molecular symmetry. Alternate atoms in the ring lie in two planes separated by about 1.3 Å, with the four atoms in each plane at the corners of a square. Bonding within the rings is covalent, and between the rings, van der Waals. The vitreous form is readily obtained on cooling the liquid, with the glass transition of about 40°C.

Crystalline selenium thus has two molecular configurations—chains and eight-membered rings—and thinking on the amorphous phase has been dominated by attempts to describe the structure in terms of these two forms. Hendus[1] was the first to determine a RDF for amorphous selenium, and he compared the results with the structure of hexagonal selenium. Krebs and Schultze-Gebhardt[2] used combined x-ray data from copper and silver radiation, and characterized the resultant structure as a combination of both eight-membered and higher-molecular-weight rings. Grimminger *et al.*[3] postulated a chain structure at room temperature and a six-membered ring at −180°C. Andrievskii *et al.*[4] used an electron-diffraction technique at various temperatures between 20 and 70°C, and concluded that eight-membered rings existed at 20°C and short chains at 70°C, with equal quantities of chains and rings present at 30 to 40°C. A very recent investigation by Henninger *et al.*[5] used both x-ray and neutron diffraction, and concluded that the structure consisted of a random arrangement of chains. However, there was a significant difference between their neutron and their x-ray results. On the other hand, new data on infrared and Raman spectra[6] have been interpreted as indicating that amorphous selenium consists of a mixture of eight-member rings and polymeric chains.

It is thus evident that there is no general agreement on the structure of amorphous selenium. With one exception,[5] the interpretation of the diffraction data is severely limited by the spurious detail in the experimental distribution functions, and in the latter case there is a notable difference between the x-ray and the neutron data. We have taken a somewhat different approach in our work, which has followed the technique we have used in studies of liquids. Two x-ray radiations were used, and a corrected RDF was derived by means of a computer-based iterative correction procedure which results in a distribution function of some reliability. The same procedure was used to obtain an experimental RDF from polycrystalline hexagonal selenium. This allowed a direct comparison with the amorphous data. The RDF curves for the $\alpha$ and $\beta$ monoclinic forms were calculated from the published crystal structures, using a Gaussian broadening function to describe the thermal motions of the atoms,[7] and we thus had distribution functions for all of the established molecular arrangements in the particular crystal structures. No one group or combination of groups in microcrystalline form reproduced the observed RDF to our satisfaction. Finally, we set up a group of 100 atom positions in a computer array, using starting positions which consisted in turn of the hexagonal and the two monoclinic atomic sites. A Monte Carlo procedure was used to move atoms from the initial sites, but a given move was only allowed if the resultant RDF was closer to the experimental curve. Reasonably good fits were obtained after about $10^5$ moves, and this permitted a choice of a most probable structure. In Sec. III, we make use of recent infrared and Raman data in an effort to characterize the basic atomic configurations in vitreous selenium.

## II. EXPERIMENTAL METHODS

### A. Materials and Apparatus

Vapor-deposited amorphous-selenium samples were prepared at the Xerox Research Laboratory. These samples were approximately 500$\mu$ thick and were made by depositing high-purity selenium on an aluminum substrate. A cast sample was prepared by melting high-purity selenium (99.999+) in an evacuated Vycor tube at 525°C and quenching the tube into ice water. The selenium was then ground to −325 mesh, and the powder was compressed in a die to form a briquette $1\times\frac{1}{2}\times\frac{1}{8}$ in. thick. There was no x-ray evidence of crystallinity in the resultant sample. Polycrystalline hexagonal samples were prepared by sintering the powder in a helium atmosphere at 185°C for 2 h and cooling slowly to room temperature. x-ray diffraction photograms failed to reveal preferred orientation in the polycrystal or the presence of any of the amorphous phase.

Two x-ray wavelengths and two diffraction geometries in reflection were used in order to obtain sufficiently extended data. At low values of the diffraction vector, $k=0.6$ to 6 Å$^{-1}$, where $k=(4\pi\sin\theta)/\lambda$, $\theta$ is the Bragg angle, and $\lambda$ is the x-ray wavelength, Co $K\alpha$ radiation was used with a LiF monochromator in the incident

[1] H. Hendus, Z. Physik **119**, 265 (1942).

[2] H. Krebs and F. Schultze-Gebhardt, Acta Cryst. **8**, 412 (1955).

[3] H. Grimminger, H. Gruninger, and H. Richter, Naturwiss. **42**, 256 (1955).

[4] A. I. Andrievskii, I. D. Nabitovitch, and Ya. V. Voloshchuk, Kristallografiya **5**, 369 (1960) [English transl.: Soviet Phys.—Crist. **5**, 349 (1960)].

[5] E. H. Henninger, R. C. Buschert, and L. Heaton, J. Chem. Phys. **46**, 586 (1967).

[6] G. Lucovsky, A. Mooradian, W. Taylor, G. B. Wright, and R. C. Keezer, Solid State Commun. **5**, 113 (1967). Additional data at liquid-helium temperature on the Raman spectrum of trigonal, $\alpha$-monoclinic, and amorphous selenium were presented by A. Mooradian and G. B. Wright at the First International Conference on the Physics of Selenium and Tellurium, Montreal, October 1967 (unpublished).

[7] R. Kaplow, S. L. Strong, and B. L. Averbach, J. Phys. Chem. Solids **25**, 1195 (1964).

beam and a proportional counter detector arranged to eliminate $\frac{1}{2}\lambda$ contributions. For the high-$k$ region 2 to 15 Å$^{-1}$, Rh $K\alpha$ was used with a LiF monochromator in the diffracted beam and a scintillation counter as the detector. The latter arrangement was particularly effective in eliminating Compton modified scattering at the higher scattering angles. Data at liquid-nitrogen temperature were obtained with a special dewar chamber, using a helium atmosphere to prevent condensation. The temperature of the specimen was measured directly with a thermocouple; temperature fluctuations during a run were less than 3°C.

The diffractometers were aligned and calibrated with a silver-powder specimen. Low index peaks had a width at half-maximum of about 20 min in $2\theta$, and all of the peak positions were within 6 min of the calculated values. In the case of amorphous samples, two passes were made over the low-angle region and four over the high-angle region, with alternate directions for the passes. The data for the hexagonal powder sample were obtained entirely with Rh $K\alpha$ radiation, using multiple passes and point counting.

### B. Analysis of Data

The measured intensity was corrected for background, polarization, and Compton scattering. The corrected intensity was expressed in electron units by determining a normalization constant such that the corrected scattering modulated the scattering function $ff^*$, where $f$ is the scattering factor and $f^*$ the complex conjugate. The normalization constant was determined separately for each radiation, and the resultant fit of the data in the overlapping regions was excellent.

We define a reduced-intensity function

$$F(k)=k(I/ff^*-1)=\int_0^\infty 4\pi r\{\rho(r)-\rho_0\}\sin krdr, \quad (1)$$

where $\rho(r)dr$ is the number of atoms per unit volume in the spherical shell between $r$ and $r+dr$, and $\rho_0$ is the average number of atoms per unit volume. A Fourier inversion yields the reduced radial distribution function

$$G(r)=4\pi r\{\rho(r)-\rho_0\}=(2/\pi)\int_0^\infty F(k)\sin krdk. \quad (2)$$

In practice, $F(k)$ was calculated directly from the corrected and normalized intensity in electron units, and a Fourier transform was used to obtain a first value of $G(r)$. This first set of functions was then treated with the error-correcting procedures. The technique for handling these corrections was devised for the treatment of data from liquids, and more complete descriptions are given in these references.[7–9] A summary of the principal features of the correction is given here.

[8] R. Kaplow, S. L. Strong, and B. L. Averbach, Phys. Rev. **138**, A1336 (1965).

[9] R. Fessler, R. Kaplow, and B. L. Averbach, Phys. Rev. **150**, 34 (1966).

Errors in the reduced-intensity function $F(k)$ may arise from such effects as an incorrect normalization constant, poor values of the coherent and incoherent scattering factors, sample roughness, and inadequate absorption corrections. These errors may be additive or multiplicative, but they are almost always slowly varying functions of $k$. The transform of a slowly varying error in $F(k)$ introduces large oscillations in the resultant transform $G(r)$, and these oscillations are localized in the region between the origin and the first peak in $G(r)$. We may assume, however, that $\rho(r)$ is zero in the region well before the first peak in the RDF, and $G(r)$ is thus linear, with an initial slope $-4\pi\rho_0$. By requiring the initial portion of $G(r)$ to be linear, the transform of the spurious oscillations may be determined and used to correct the experimental $F(k)$. The final smoothed experimental initial slope can be used to determine $\rho_0$, and this has invariably been in good agreement with the bulk determinations of density.

A rigorous transform of $F(k)$ requires that the data extend to infinite scattering angles, or at least until $F(k)$ is very close to zero. Since the experimental $F(k)$ terminates at some value $k_{\max}$ which does not meet this requirement, the resultant $G(r)$ has a termination error. Unfortunately, the termination produces oscillations in the transform which are located in the vicinity of the first peak in $G(r)$, and this type of error has been the cause of a great deal of uncertainty in the resultant RDF. We correct for the termination error by analytically extending the experimental $F(k)$ beyond the value of $k_{\max}$ in such a way as to meet the following requirements: (a) The transform of the final $G(r)$ function must reproduce the measured $F(k)$ up to $k_{\max}$, and (b) $G(r)$ must be linear below the first peak. The termination correction is made by arbitrarily limiting the measured $F(k)$ at three different values of $k$ and noting the effect in the resultant $G(r)$. An estimate of the proper $G(r)$ is then made, and the corrected function is transformed to give a new $F(k)$. This procedure is repeated until a self-consistent extension of $F(k)$ subject to the requirements given above is obtained, and we have found that this function need only be extended to a value of $k=2k_{\max}$ in order to give satisfactory $G(r)$ functions. Although we have been unable to show analytically that the resultant extension to $F(k)$ is unique, we have returned consistently to the same corrected function even after using significantly different initial corrections to $G(r)$.

## III. DISCUSSION OF RESULTS

### A. Hexagonal Selenium

Let us first consider the RDF for polycrystalline hexagonal selenium. This crystal structure contains parallel helical chains of selenium atoms at the corners and center of a hexagon, and these chain units are frequently considered to be present in the amorphous structure. The corrected experimental reduced RDF

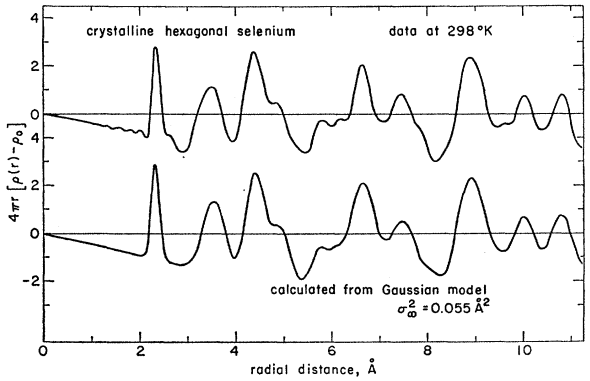


FIG. 1. Reduced radial distribution function and calculated function from Gaussian model of crystalline hexagonal selenium.

$G(r)$ is shown in the upper portion of Fig. 1. The first two peaks are quite well resolved, and we may obtain the corresponding number of neighbors from the total radial density function $J(r)=4\pi r^2\rho(r)$. The number of neighbors in the $i$th shell, $C_i$, is obtained from

$$C_i=\int_{r_i-\Delta}^{r_i+\Delta} 4\pi r^2\rho(r)dr. \qquad (3)$$

The resultant coordination parameters are listed in Table I, and it is evident that there is good agreement with the published data on hexagonal selenium.[10] This procedure is not useful beyond a few nearest neighbors because the shells of atoms begin to overlap considerably.

The broadening of the peaks in the RDF for the crystalline material is produced by thermal vibration. We may thus start with the known atomic positions in the crystal, introduce a suitable thermal-frequency spectrum, and attempt to reproduce the measured RDF. Our earlier work on metallic crystals[7] has shown that the average thermal vibrations may be represented by a Gaussian distribution function in the form

$$4\pi r^2\rho(r)=\sum_{i=1}^{\infty}\frac{C_i}{(2\pi\sigma_i^2)^{1/2}}\exp\left[\frac{(r-r_i)^2}{2\sigma_i^2}\right], \qquad (4)$$

where $C_i$ is the number of atoms in the $i$th shell about an arbitrary atom as the origin, $r_i$ is the distance from the origin to the $i$th shell, and $\sigma_i^2$ is the mean-square amplitude of vibration between the atom at the origin and atoms in the $i$th shell.

Ideally, the values of $\sigma_i$ should be computed from a frequency spectrum for the lattice, but alternatively, they may be determined as parameters in the fitting procedure. We define coupling coefficients $\gamma_i$, which range from zero to unity, as

$$\gamma_i=\sigma_i^2/\sigma_\infty^2, \qquad (5)$$

where $\sigma_\infty$ is the amplitude of vibration between atoms at infinite separation; it is assumed that atoms at infinite separation vibrate independently of each other. A coupling coefficient of unity thus indicates independent, or uncoupled, vibration. A zero coefficient indicates that the motions of the atoms at the corresponding separation $r_i$ are completely coupled. We have obtained a set of coupling coefficients and the mean-square amplitude $\sigma_\infty^2$ by starting with the known atomic positions and using Eq. (4) to obtain the best fit to the measured RDF. No constraints were put on the permissible values of $\gamma_i$ and $\sigma_\infty$, and Fig. 1 shows that the resultant fit between the measured and the calculated RDF is very close.

A value of $\sigma_\infty^2=0.055$ Å$^2$ was used in the final match at room temperature, and the corresponding coupling coefficients are listed in Table II. It is evident that two sets of coupling coefficients are involved. The coefficients for atoms along a chain, which are indicated with a superscript "a" in Table II, start with a very low value for the nearest neighbors, i.e., $\gamma_1=0.13$, and progress systematically to unity at a separation of about 6.8 Å. On the other hand, the other distances listed in Table II, which are interchain distances, start with a largely uncoupled value, i.e., $\gamma=0.70$, and these atoms

TABLE I. Coordination in hexagonal selenium.

| | This work | Accepted value |
|---|---|---|
| Interatomic distances (Å) | | |
| $r_1$ | 2.32 | 2.324 |
| $r_2$ | 3.55 (unresolved) | 3.47<br>3.68 |
| Number of neighbors | | |
| $C_1$ | 2.0 | 2.0 |
| $C_2$ | 5.8 (unresolved) | 4 at 3.47<br>2 at 3.68 |

TABLE II. Coupling coefficients for hexagonal selenium at room temperature. $\sigma_\infty^2=0.055$ Å$^2$.

| Interatomic separation $r_i$ (Å) | Coupling coefficients $\gamma_i$ |
|---|---|
| 2.32[a] | 0.13 |
| 3.47 | 0.70 |
| 3.68[a] | 0.55 |
| 4.36 | 0.65 |
| 4.49 | 0.75 |
| 4.93 | 0.85 |
| 4.95[a] | 0.65 |
| 5.70 | 0.70 |
| 6.06 | 0.90 |
| 6.13 | 0.75 |
| 6.59 | 0.95 |
| 6.70 | 1.00 |
| 6.77 | 1.00 |
| 6.80[a] | 1.00 |
| 7.06 | 1.00 |
| 7.27 | 0.90 |
| 7.52 | 0.90 |
| 7.54 | 0.95 |

[a] Intrachain distance; the others are interchain distance.

[10] R. Wyckoff, *Crystal Structures* (Interscience Publishers, Inc., New York, 1963), 2nd ed., Vol. I.

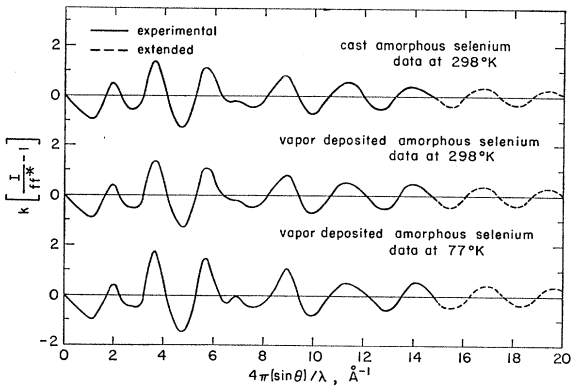


FIG. 2. Reduced-intensity functions for amorphous selenium.

remain comparatively uncoupled at all atomic separations. Thus the covalently bonded atoms along the chain are strongly coupled, whereas the van der Waals coupling between chains is quite weak. It should be emphasized that this separation of coefficients comes directly from the analysis and was not introduced *a priori*.

We may express the mean-square deviation from the lattice position, $\langle u_s^2\rangle_{\text{av}}$, which appears in the Debye-Waller factor, as $\sigma_\infty^2=\langle 2u_s^2\rangle_{\text{av}}$ and calculate the Debye temperature from the usual Debye function.[11] Using the value $\langle u_s^2\rangle_{\text{av}}=0.0275$ Å$^2$, the resultant Debye temperature is $141\pm4$°K, and this compares well with the average value in the literature, 135°K.

The data on hexagonal selenium thus establish the form of the RDF for this crystalline form and provide a set of coupling coefficients which adequately describe the thermal spectrum in this material. The resultant agreement between the measured and the calculated RDF (Fig. 1) also provides some confidence in using this technique to generate an RDF for the other crystalline forms of selenium.

### B. Amorphous Selenium

The reduced-intensity functions $F(k)$ are shown in Fig. 2 for the cast amorphous sample, the vapor-deposited sample at room temperature, and the vapor-deposited sample at liquid-nitrogen temperature. The two room-temperature samples resulted in almost identical scattering curves despite the differences in the method of preparation. The data obtained at the lower temperature exhibited a slight sharpening of the peaks. The corresponding reduced radial density functions $H(r)=4\pi r^2\{\rho(r)-\rho_0\}$ are shown in Fig. 3. The efficacy of the correction is indicated by the smooth parabolic form of the curve in the region before the first peak and the relative absence of sharp oscillations in the vicinity of the first peak. The dashed section of Fig. 2 indicates the extension to the experimental curve which results from the correction procedure. It is felt that the shapes of the reduced radial density functions in Fig. 3 are meaningful, and that a model of the amorphous structure should be capable of reproducing the distribution. Note that we have plotted the reduced radial density function $H(r)$ in Fig. 3. In contrast, the radial distribution function $G(r)$ is plotted for the hexagonal material in Fig. 1 in order to avoid the very large magnification of the crystalline peaks at large values of $r$. The positions of the peaks in these two functions are essentially the same, but the ordinates in Fig. 1 must be multiplied by $r$ to give a quantitative comparison of the number of atoms.

A comparison of Figs. 1 and 3 shows that the first two peaks of the amorphous structure are about as sharp as the corresponding hexagonal peaks. Table III summarizes the positions of the first two peaks $r_1$ and $r_2$ and the corresponding number of atoms $C_1$ and $C_2$. The number of atoms was obtained by measuring the half-width of each peak on the lower side and constructing a Gaussian curve with the observed maximum value. The area under the Gaussian curve was then assumed to represent the number of atoms at the distance corresponding to the peak position; the widths of the Gaussian curves then correspond to the relative displacements $\langle\sigma_1^2\rangle_{\text{av}}$ and $\langle\sigma_2^2\rangle_{\text{av}}$. The data in Table III indicate that the first and second neighbors are slightly farther out than in the hexagonal structure, that the number of first and second neighbors is about the same for the two structures, and that the thermal vibrations for the first two shells are remarkably similar in both

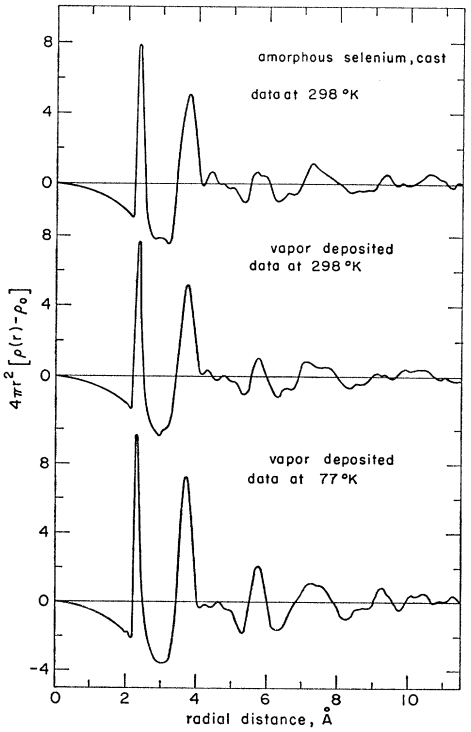


FIG. 3. Radial distribution functions for amorphous selenium.

[11] R. W. James, *The Optical Properties of the Diffraction of X Rays* (G. Bell and Sons, London, 1948).

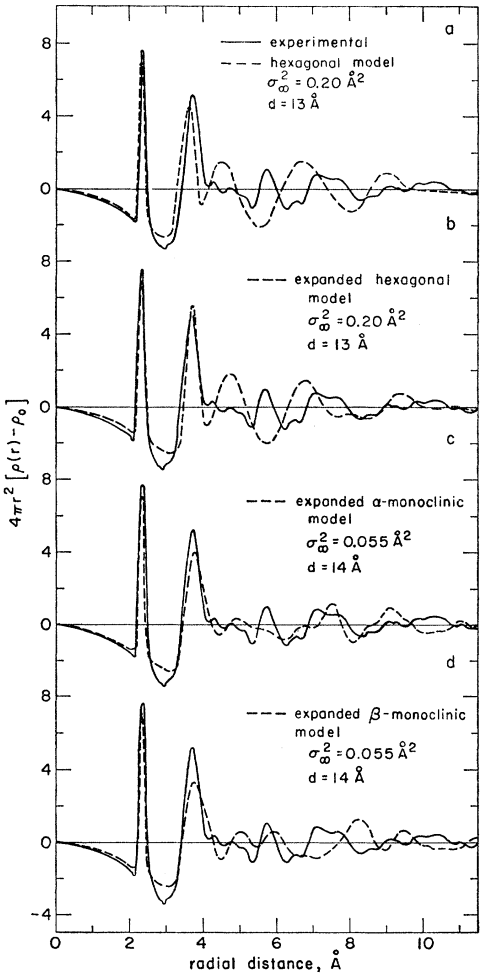


FIG. 4. Microcrystalline models for amorphous selenium.

structures at room temperature. Note that the second peak in the crystalline distribution function includes two atomic shells, and the values of $\langle\sigma_2^2\rangle_{av}$ listed in Table III refer to the width of the unresolved peak.

The positions of the principal peaks facilitate a comparison with other data on amorphous selenium. The peak positions in this work were chosen primarily from the vapor-deposited amorphous sample at room temperature (Fig. 3, middle curve), but they correspond very closely to the results from the cast sample. The data at low temperature exhibit somewhat greater resolution, and were very helpful in establishing the validity of each peak, but the positions are slightly different because of the normal contraction on cooling. These principal coordination distances are listed in Table IV and compared with the corresponding x-ray and neutron data obtained by Henninger *et al.*[5] There is excellent agreement for the first two peaks. However, we do not exhibit a peak at 4.62 Å; their x-ray data show such a peak, but their neutron data do not. We also show peaks at 5.8 and 7.2 Å, and our additional peaks beyond these distances are a consequence of our confidence in the significance of the bumps in the RDF at these distances. The peak at 4.62 Å corresponds to a strong peak in the hexagonal structure (Fig. 1), and we conclude that their thin vapor-deposited x-ray sample was probably crystallized in part. Surface crystallization, if it were present, would play a small part in the massive sample used for their neutron experiment, but it would affect their x-ray results significantly. We thus believe that their third peak at 4.62 Å is not a feature of the amorphous structure.

TABLE III. Near-neighbor correlations in amorphous selenium.

| Sample | Interatomic distances (Å) $r_1$ | $r_2$ | Number of atoms $C_1$ | $C_2$ | Relative displacements (Å²) $\langle\sigma_1^2\rangle_{av}$ | $\langle\sigma_2^2\rangle_{av}$ |
|---|---|---|---|---|---|---|
| Cast | 2.34 | 3.75 | 2.0 | 6.4 | 0.007 | 0.058 |
| Vapor-deposited | 2.34 | 3.75 | 2.0 | 6.3 | 0.007 | 0.056 |
| Vapor-deposited data at 77°K | 2.31 | 3.70 | 2.0 | 6.6 | 0.006 | 0.040 |
| Hexagonal | 2.32 | 3.55 | 2.0 | 5.8 | 0.007 | 0.055 |

TABLE IV. Principal correlation peaks in amorphous selenium at room temperature (Å). Peaks 2a, 2b, and 2c are minor peaks relative to the principal peaks, but still significant. Peak 3′ appears only in the x-ray data of Henninger *et al* (Ref. 5).

| Peak number | Henninger *et al.*[a] X-ray | Neutron | This work |
|---|---|---|---|
| 1 | 2.33 | 2.33 | 2.34 |
| 2 | 3.73 | 3.71 | 3.75 |
| 2a | ... | ... | 4.3 |
| 2b | ... | ... | 4.7 |
| 2c | ... | ... | 5.1 |
| 3′ | 4.62 | ... | ... |
| 3 | 5.8 | 5.74 | 5.8 |
| 4 | 7.2 | 7.25 | 7.2 |
| 5 | ... | ... | 7.7 |
| 6 | ... | ... | 9.3 |
| 7 | ... | ... | 10.0 |
| 8 | ... | ... | 10.5 |

[a] Reference 5.

## IV. AMORPHOUS STRUCTURE

It is apparent that correlation distances beyond the first two nearest neighbors must be considered in order to describe the structure of selenium. The interatomic distances for the hexagonal, $\alpha$-monoclinic, and $\beta$-monoclinic structure are summarized, along with the principal correlation distances in the amorphous structure, in Table V. There are very small differences in interatomic distances between the chain (hexagonal) and the ring (monoclinic) structures until distances beyond the third nearest neighbors are reached, and it is evident that the RDF of the amorphous structure

TABLE V. Principal intramolecular correlation distances in rings and chains (Å).

| Amorphous, experimental | Linear chain, hexagonal | Eight-atom ring, monoclinic |
|---|---|---|
| 2.34 | 2.32 | 2.34 |
| 3.75 | 3.68 | 3.72 |
| ... | 4.95 | ... |
| ... | ... | 5.01 |
| ... | ... | 5.24 |
| 5.8 | ... | ... |
| ... | 6.80 | ... |
| 7.2 | ... | ... |
| ... | 8.41 | ... |
| 9.2 | ... | ... |

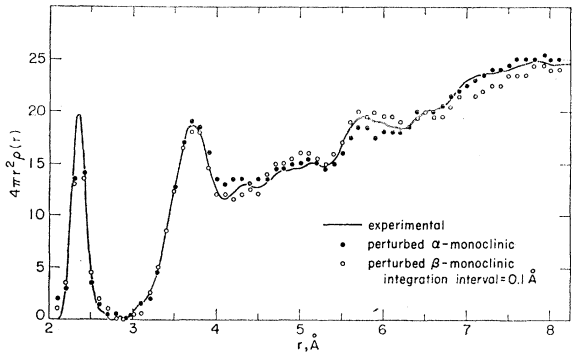


FIG. 5. Radial density function for amorphous selenium calculated from perturbation of α-monoclinic ring structure.

requires a more complete description than a specification of the first few neighbor populations. The experimental correlation functions exhibit strong correlations at distances up to about 10 Å, and it thus appears that the arrangement of the molecular units exhibit considerable local order.

A number of attempts were made to devise a model of the amorphous structure. The first model assumed that the amorphous structure consisted of randomly oriented microcrystals of the hexagonal structure. It was postulated that the arrangement of chains in each microcrystal was that of the hexagonal structure, but the size of the microcrystals and the thermal displacements were left as free parameters. This procedure has been used quite successfully to describe the structure of liquid lead and mercury,[8] as well as aluminum.[9] Figure 4(a) shows the result for the hexagonal microcrystal, and it is apparent that there is an obvious difficulty with the position of the second peak; this arises because the hexagonal structure is slightly denser than the amorphous form. The hexagonal structure was expanded slightly, according to the parameters listed in Appendix A, by keeping the distances within the chain constant, but increasing the distances between the chains. Figure 4(b) shows that this expanded crystalline model has fairly good coincidence over the first two peaks, but that there are serious discrepancies beyond. A mean-square amplitude $\langle\sigma_\infty^2\rangle_{av}=0.20$ Å$^2$ was required to obtain even this inadequate fit, and this is far greater than the value $\langle\sigma_\infty^2\rangle_{av}=0.055$ Å$^2$ measured for the thermal vibrations in the hexagonal material. It thus appears that rather large static atomic displacements are required, in addition to the usual thermal displacements, in this effort to describe the amorphous structure as microcrystals of the hexagonal chain structure, and even then the resultant fit is poor. A crystallite diameter, or critical correlation distance, of $d=13$ Å was required to obtain the proper damping; this value is close to the values obtained for liquids.

Similar attempts were made to fit the amorphous structure with microcrystalline forms of the monoclinic ring structures. Figure 4(c) shows that an expanded α-monoclinic microcrystalline model fits rather well, except for a poor fit in the region of 5.7 Å. The parameters of the expanded α-monoclinic structure are listed in the Appendix A, and the expansion comes only in increasing the distances between the rings. A reasonably good fit was obtained by using a thermal amplitude $\langle\sigma_\infty^2\rangle_{av}=0.055$ Å$^2$, a value identical with the experimental measurement for the hexagonal crystalline structure. The resultant coupling factors, which are listed in Table VI, are quite close to the values listed in Table II for the hexagonal crystalline material. Similarly, the expanded β-monoclinic microcrystalline model (see Appendix A for the expanded cell parameters) also fits reasonably closely, but there is a serious mismatch in the region 7–9 Å. The corresponding model parameters are also listed in Table VI. It is evident that none of the microcrystalline models fits closely enough to adequately describe the amorphous structure. This does not rule out the presence of chains or rings in the amorphous arrangement, but the particular arrangement of rings and chains in these crystalline structures cannot persist in the glassy state. Nevertheless, the fit with the

TABLE VI. Parameters for quasicrystalline models. $d$ is the critical correlation distance; $\langle\sigma_\infty^2\rangle_{av}$ is the mean-square thermal amplitude between atoms at infinite separation; $\gamma_i$ are the coupling factors between atom displacements for the $i$th neighbor.

| | Hexagonal | Expanded hexagonal | Expanded α-monoclinic | Expanded β-monoclinic |
|---|---|---|---|---|
| $d$ (Å) | 13 | 13 | 14 | 14 |
| $\langle\sigma_\infty^2\rangle_{av}$ (Å$^2$) | 0.20 | 0.20 | 0.055 | 0.055 |
| $\gamma_1$ | 0.03 | 0.03 | 0.06 | 0.06 |
| $\gamma_2$ | 0.15 | 0.30 | 0.50 | 0.50 |
| $\gamma_3$ | 0.07 | 0.10 | 0.50 | 0.50 |
| $\gamma_4$ | 0.80 | 0.80 | 0.60 | 0.60 |
| $\gamma_5$ | | | 0.60 | 0.60 |
| $\gamma_6$ | | | 0.70 | 0.70 |
| $\gamma_7$ | | | 0.70 | 0.70 |
| $\gamma_8$ | | | 0.70 | 0.80 |
| $\gamma_9$ | | | 0.80 | 0.80 |
| $\gamma_{10}$ | | | 0.80 | 0.80 |
| $\gamma_{11}$ | | | 0.80 | 0.90 |
| $\gamma_{12}$ | | | 0.90 | 0.90 |
| $\gamma_{13}$ | | | 0.90 | 0.90 |

TABLE VII. Grouping of atoms in perturbed $\alpha$-monoclinic structure (rings) in a 100-atom spherical sample.

| Initial structure | | Perturbed structure | |
|---|---|---|---|
| Number of groups | Atoms in each group | Number of groups | Atoms in each group |
| 6 | 8 | 1 | 9 |
| 2 | 7 | 5 | 8 |
| 2 | 4 | 1 | 7 |
| 6 | 3 | 1 | 6 |
| 2 | 2 | 2 | 4 |
| 8 | 1 | 4 | 3 |
| | | 4 | 2 |
| | | 10 | 1 |

$\alpha$-monoclinic microcrystalline model is probably the closest seen thus far, and it would thus seem that this would constitute some evidence for the presence of rings in the amorphous structure, but it must be conceded that these rings are probably not in the same exact arrangement as in the $\alpha$-monoclinic form. Attempts to describe the structure by using fractions of the expanded hexagonal and monoclinic forms were also not very satisfactory in fitting the experimental density functions. Thus it seems that if the amorphous structure contains rings and chains, the packing arrangement of these molecular units must be different from that of the crystalline forms.

A Monte Carlo procedure was finally adopted to fit the experimental RDF. Atom positions were arranged in a computer array corresponding to one of the crystalline structures, for example, the $\alpha$-monoclinic. The expanded $\alpha$-monoclinic form was used (Appendix A), so that the density of the starting structure was equivalent to that of the amorphous material. A spherical sample consisting of 100 atoms was used, and the actual number of nearest neighbors in the sample was used in generating the RDF from these models. An atom, chosen at random, was then moved, and the resultant RDF was then compared with the measured value. If the match was improved, the move was allowed to remain; if the match was not improved, the atom was returned to the original position. Atom centers were not permitted to move closer than the measured distance of closest approach, but there were no other restrictions on the motion. The comparison was made with the experimental radial density function $J=4\pi r^2\rho(r)$, multiplied by a damping function which gives the fractional number of bond ends which terminate within a sphere containing 100 atoms, as a function of the correlation distance. The modified experimental radial density function, shown as the solid curves in Figs. 5 and 8, thus represents the total radial density that would be found if a sphere containing an average group of 100 atoms were removed from the sample and measured in isolation. This approach eliminates the uncertainties associated with the cyclic or periodic boundary conditions which are usually used in calculations from models with a small number of atoms.

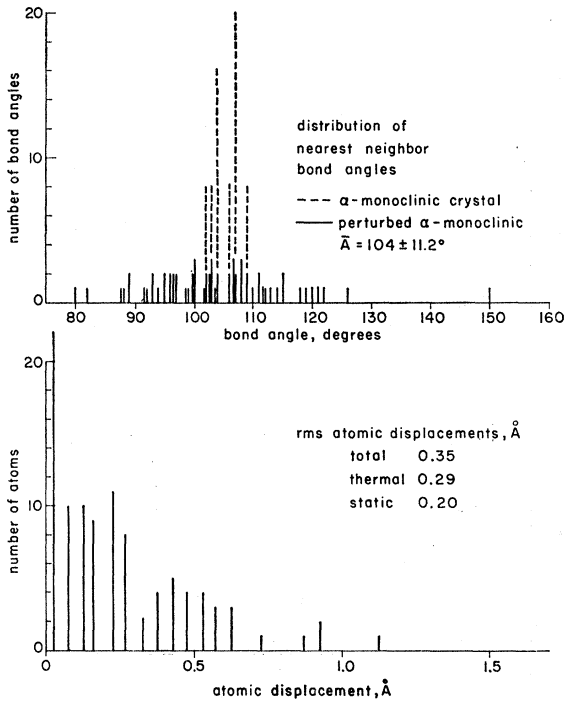


FIG. 6. Perturbed $\alpha$-monoclinic structure (rings).

Approximately $10^5$ moves were made before the model became locked in to the point where additional moves no longer improved the fit significantly. The following procedure was also found to be helpful in arriving at rapid convergence. For the early moves, the radial density function was calculated using a rather broad integration interval, $\Delta r=0.2$ Å. After the atoms had moved close to the final positions, a finer interval, $\Delta r=0.1$ Å, was used, and our final results are presented for this integration interval. In a few cases an even finer interval, $\Delta r=0.05$ Å, was used, but this did not materially change the results. In practice, the coarse interval favored a rapid convergence, whereas the finer interval was required to ensure an adequate description of the first peak. After the fit could no longer be improved, we examined the final positions of the atoms and attempted to deduce the structure.

The resultant fit for the perturbed $\alpha$-monoclinic structure is shown by the solid points in Fig. 5. Although there are local deviations from the experimental structure, it is evident that the radial density function has been reproduced quite well. A look at the perturbations, which are summarized in Fig. 6, is quite revealing. The total rms displacement in the model is $\langle u_{\text{total}}^2\rangle_{\text{av}}^{1/2}=0.35$ Å, and the distribution of the atomic displacements is skewed toward small displacements. The total three-dimensional amplitude for thermal vibrations in the hexagonal form is $(3\langle u_s^2\rangle_{\text{av}})^{1/2}=\langle u_{\text{thermal}}^2\rangle_{\text{av}}^{1/2}=0.287$ Å. If we assume the same vibrational amplitudes for the amorphous form, the net mean-square

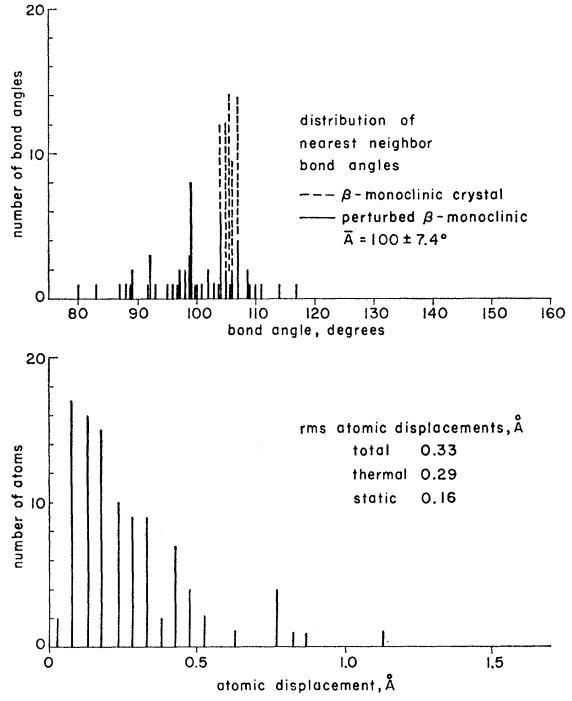


FIG. 7. Perturbed $\beta$-monoclinic structure (rings).

static displacement is $\langle u_{\text{total}}^2\rangle_{\text{av}} - \langle u_{\text{thermal}}^2\rangle_{\text{av}} = \langle u_{\text{static}}^2\rangle_{\text{av}} = 0.04$ Å$^2$. The resultant rms static displacement is $\langle u_{\text{static}}^2\rangle_{\text{av}}^{1/2} = 0.20$ Å. Thus relatively small static motions were required to convert the $\alpha$-monoclinic into the amorphous structure. Definitions of the various thermal- and static-displacement terms are given in Appendix B. The resultant bond angles are also shown in Fig. 6. The bond angles in the $\alpha$-monoclinic crystal are listed as varying from 101.6° to 109°. The mean bond angle in the perturbed $\alpha$ structure was 104°, with a mean deviation of 11.2°, and it is evident that the bond angles have not been changed very much in the amorphous model. Note that even the perfectly crystalline hexagonal structure must exhibit a spread in bond angles, because of thermal vibrations. Roughly, the root-mean-square deviation of the angle $\langle \Delta A^2\rangle_{\text{av}}^{1/2}$, in the hexagonal form for which we have some experimental vibrational data, can be estimated from the sum of the relative vibrational amplitudes of the first- and second-neighbor intrachain bonds as $\langle \Delta A^2\rangle_{\text{av}}^{1/2} \approx [0.055(0.13+0.55)]^{1/2}/r_1 \approx 5°$. Such a comparison is more difficult with the monoclinic structures, in part because we do not have the corresponding experimental quantities, and in part because the published atomic positions indicate a significant spread in bond angles $\langle \Delta A^2\rangle_{\text{av}}^{1/2} \approx 2°$, even without considering thermal vibrations.

TABLE VIII. Grouping of atoms in perturbed $\beta$-monoclinic structure (rings) in a 100-atom spherical sample.

| Initial structure | | Perturbed structure | |
|---|---|---|---|
| Number of groups | Atoms in each group | Number of groups | Atoms in each group |
| 2 | 8 | 2 | 8 |
| 2 | 7 | 2 | 7 |
| 10 | 5 | 10 | 5 |
| 2 | 4 | 2 | 4 |
| 4 | 2 | 3 | 2 |
| 4 | 1 | 6 | 1 |

It is also interesting to note that the width of the nearest-neighbor peak in the amorphous phase is virtually identical to that in the hexagonal crystalline form. Therefore the static displacements associated with most nearest-neighbor bonds must be negligible.

We may further examine the final atomic arrangement in the perturbed $\alpha$-monoclinic structure, and the atomic groupings in the model are summarized in Table VII. The original configuration contained six complete eight-member rings. The other atoms were in parts of rings terminated by the spherical surface. In the final configuration we found two types of perturbations. The complete rings exhibited slight distortions, and in one typical case the plane which contains four of the atoms in the ring had tilted relative to the plane which contains the other four atoms. These planes are normally parallel, with a separation of approximately 1.3 Å; at the tilted corner the separation was approximately 1.8 Å. Most of the eight-member rings were distorted in this fashion. However, one ring which started with seven atoms (the eighth atom was cut off by the surface of the model) had opened slightly and moved closer to another partial ring of three atoms. The normal nearest-neighbor separation is about 2.3 Å, but the separation at the opening was about 3.5 Å. The atoms in the vicinity of the opening had an arrangement which was similar to the end of a chain, with a local trigonal symmetry, but even here the configuration was closer to a ring than a chain. Thus, of the 100 atoms in the model, only about four atoms exhibited localized trigonal symmetry, and the rest were in eight-member rings.

A rather similar result was obtained on starting with rings in the $\beta$-monoclinic arrangement. The open circles in Fig. 5 show the resultant fit, and it appears to be as good as the $\alpha$ perturbation. The atomic displacements and the final bond angles (Fig. 7) are rather similar to the $\alpha$ model; the net static displacement was 0.16 Å, and the final bond angle was 100°, with a mean deviation of 7.4°. Table VIII shows that the initial and final atomic configurations are almost identical. The $\alpha$- and $\beta$-monoclinic forms are very similar, and relatively little difference in the resultant perturbations should be expected.

Starting with atoms in hexagonal positions, however, produced somewhat different results. Figure 8 shows the final fit to the experimental structure, and it is evident that the match is not quite so good as in the monoclinic models. The perturbations required were very large. Figure 9 shows that the mean atomic displacements were 0.74 Å, with 19 atoms moving more than 1 Å.

These large atomic excursions were not made by single unattached atoms in the original configuration, but, with only one exception, involved atoms whose nearest neighbors were present in the sample. The bond angle in the hexagonal crystal is 105°, and Fig. 9 shows that this bond angle is greatly perturbed in the final arrangement, varying from 78° to 163°, with a mean value of 116° and a standard deviation of 19.9°. Only 13 angles of a total of 56 were in the interval 105°±5°. The final atomic grouping in the hexagonal model is summarized in Table IX. There was one large grouping of 24 atoms which was made up of atoms from four neighboring parallel chains in the original hexagonal starting positions. These chains were joined where atoms had moved into positions between the two chains and had created local regions which looked very much like rings. The chain structure was still well developed, but there were definite indications of ring formation.

It is instructive to examine the reasons for the failure of the microcrystalline model to reproduce the amorphous radial distribution as well as the perturbed structures. The microcrystalline model requires the maintenance of the lattice symmetry along with the molecular symmetry. Although fairly large atomic excursions are allowed, these are similar to the thermal vibrations in that the crystalline symmetry must be maintained; the correlation range is defined independently from the atomic motions, in terms of the crystallite size. Thus the chains in the hexagonal microcrystal must remain straight and parallel, with substantially the original bond angles. Similarly, the monoclinic microcrystal requires that the rings be virtually intact and parallel. The fact that the monoclinic microcrystalline models fit as well as they do (Fig. 4) is probably indicative that such an arrangement of rings is a close approximation to the amorphous structure. On the other hand, the perturbed structures do not have any *a priori* restrictions on the symmetry. A very small rms atomic displacement was required to convert the monoclinic selenium crystalline structures to the amorphous form. With the exception of the one pseudochain which formed in the $\alpha$ perturbation, the molecular symmetry of the $Se_8$ ring

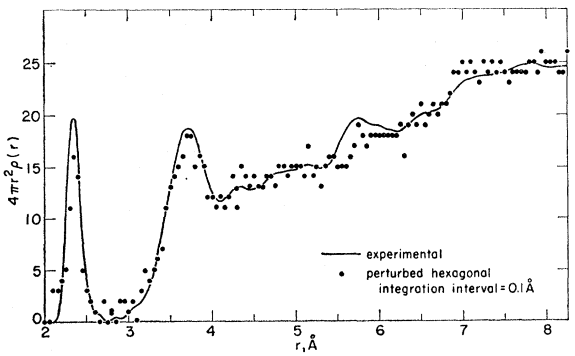


FIG. 8. Radial density function for amorphous selenium calculated from perturbation of hexagonal chain structure.

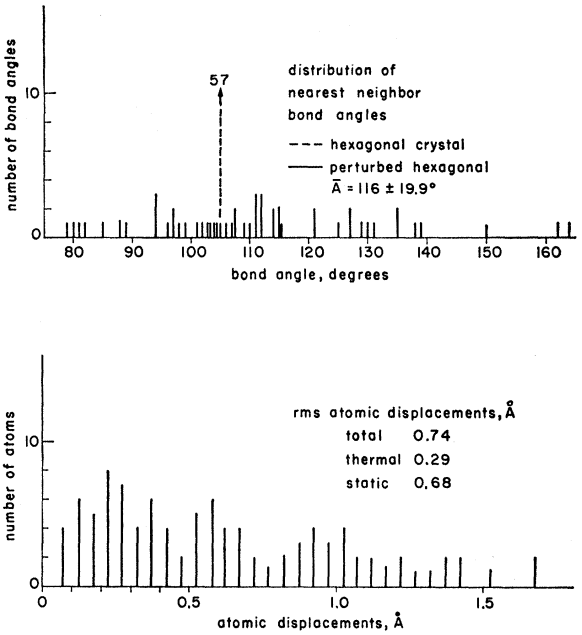


FIG. 9. Perturbed hexagonal structure (chains).

was maintained. This is also indicated by the relatively small changes which occurred in the resultant bond angles. It thus appears that the static displacements must destroy the lattice symmetry, and not the molecular group symmetry. The rings in the amorphous structure are thus distorted or tilted slightly with respect to each other, but the distortions and tilts cannot have a strict periodicity. On the other hand, considerable perturbation is required to convert the hexagonal chain structure to the amorphous form. The resultant chains are no longer straight, and there is a considerable variation in the bond angles. Trigonal symmetry is probably retained for an atom and its nearest neighbors, but with considerable deviations from strict symmetry. The correlation range is not defined separately in these perturbed models, and the limitation on correlation is an implied consequence of the destruction of the lattice symmetry by the atomic displacements.

There is also the possibility that the published nearest-neighbor distances of the monoclinic structures are somewhat in error. It seems unlikely that the slight variations listed in the nearest-neighbor distances and in the bond angles for the $Se_8$ ring are real, and we suspect that some of the atomic displacements required in the perturbed structures were required to improve the symmetry of the rings so that they would better fit the measured radial distribution function. The resultant rings in the perturbed model frequently appeared to be more regular in the amorphous model than in the listed crystal structure, and this casts some doubt on the published data for the rings. In addition, the coupling factors derived from the microcrystalline model of the ring structures indicated that the total atomic displace-

TABLE IX. Grouping of atoms in perturbed hexagonal structure (chains) in 100 atom spherical sample.

| Initial structure | | Perturbed structure | |
|---|---|---|---|
| Number of groups | Atoms in each group | Number of groups | Atoms in each group |
| 1 | 11 | 1 | 26 |
| 6 | 9 | 1 | 10 |
| 2 | 5 | 1 | 7 |
| 6 | 2 | 3 | 6 |
| 13 | 1 | 1 | 5 |
| | | 1 | 4 |
| | | 2 | 3 |
| | | 4 | 2 |
| | | 16 | 1 |

ments for the nearest neighbors in the vitreous material was about one-half that of the probable thermal displacements in the crystal. This does not seem very likely, and we conclude that the nearest-neighbor distances and bond angles for the ring structures probably do not exhibit the spread indicated in the published values.

The recent infrared and Raman spectra on amorphous selenium[6] lend considerable support to the presence of rings in the vitreous structure. There is a very broad band in the Raman spectrum at a frequency of 250 $cm^{-1}$, which probably includes the frequencies 240, 251, 256, and 264 $cm^{-1}$ corresponding to the $E_3$, $A_1$, $E_2$, and $E_1$ modes, respectively, in the $\alpha$-monoclinic ring structure. There are additional Raman lines at 50, 80, and 112 cm in the amorphous structure, corresponding to the $E_2$ and $A_1$ modes in the monoclinic. The latter lines are weak, but still well-developed. The Raman evidence for the presence of trigonal structure in the amorphous material is somewhat less certain. There are two strong Raman lines in the hexagonal material at 233 and 237 $cm^{-1}$, corresponding to the $A_1$ and $E$ trigonal modes, respectively. There is a shoulder in the Raman line of the amorphous structure at about 235 $cm^{-1}$, and this may be interpreted as evidence for the presence of the trigonal symmetry, even though the line is partially obscured by the strong lines from the ring at this frequency. The infrared data also support the presence of rings, with bands at 95 and 120 $cm^{-1}$, corresponding to the $E_1$ and the $B_2$ modes of the $Se_8$ ring. There is a weak infrared band at 135 $cm^{-1}$ which is attributable to trigonal symmetry, with vibrations in the $E$ mode. This is the only infrared band which is unequivocably associated with trigonal symmetry in the amorphous material. We thus have very strong optical evidence for the presence of $Se_8$ rings. The indications of the trigonal symmetry are weaker. The $D_3$ torsional modes ($E$) and stretch modes ($A_1$) are apparently present, but it should be pointed out that all of these modes involve only an atom and its nearest neighbors. Thus a mixture of rings and chains could account for these spectra, but if the chains were well developed, we would expect very strong evidence of the presence of the $E$ and the $A$ modes. In fact, this kind of indication is very pronounced for the $Se_8$ rings. On the other hand, the atoms in the vicinity of the opened rings in the perturbed-ring model are capable of generating the $E$ and $A_1$ trigonal modes on a local scale, and it is possible that the indications of trigonal symmetry arise from such opened rings. Thus we feel that the optical data indicate unequivocably that well-developed $Se_8$ rings exist in the amorphous structure. The weaker evidence for trigonal symmetry indicates the presence of opened rings or a few chains which are distorted into ringlike forms.

On considering our data, along with the optical results, we conclude that there is strong evidence that the structure of amorphous selenium consists mainly of $Se_8$ puckered rings, along with a few slightly opened rings which allow the atoms near the opening to exhibit a weak trigonal symmetry for a few atoms and their nearest neighbors rather than the $Se_8$ ring symmetry. Our $\alpha$ perturbation resulted in a distribution with about 95% of the atoms in ring symmetry and with about 5% in a weak trigonal symmetry, and we would tentatively assign this distribution as characteristic of the amorphous material. On the basis of the diffraction data alone, we cannot make a choice between a structure consisting entirely of slightly perturbed rings or one of considerably distorted chains. In principle, it appears that either perturbed structure could be made to reproduce the observed amorphous RDF equally well. However, the infrared and optical spectra indicate decisively that the $Se_8$ molecular group is present, with only a weak indication of a nearest-neighbor trigonal arrangement. Our $\alpha$ perturbation produced just such a structure, and we thus conclude that the structure is mainly rings, with a few localized trigonal regions near opened rings.

## V. SUMMARY

A combination of our measured radial distribution functions for amorphous selenium, our Monte Carlo models, and recent infrared and optical data suggest that vitreous selenium consists mainly of $Se_8$ rings, along with a few atoms in a weak nearest-neighbor trigonal symmetry. We suggest that approximately 95% of the atoms are in ring symmetry and about 5% in weak trigonal symmetry. The point-group symmetry of the rings is well maintained, with little change in bond angle. The weak trigonal symmetry for a few atoms and their near neighbors appears to arise either because of a slight opening in an occasional ring or because of the presence of a few greatly distorted chains.

## ACKNOWLEDGMENTS

The authors would like to acknowledge the assistance of the Xerox Corporation in sponsoring this work and the contributions of the MIT Computation Center in providing facilities for the computer calculations. We would also like to acknowledge several very interesting discussions with Dr. Peter J. Warter, Dr. Evan Felty,

Dr. G. Lucovsky, and Dr. Mark Myers at the Xerox Laboratory, and with Dr. A. Mooradian of the MIT Lincoln Laboratory.

## APPENDIX A: CRYSTALLINE FORMS EXPANDED TO AMORPHOUS DENSITY

(1) Expanded hexagonal selenium:

| $a$ | $c$ |
|---|---|
| 4.6406 Å, | 4.9495 Å. |

Altered atomic coordinates:

| $u$ | $v$ | $w$ |
|---|---|---|
| 0.2037, | 0.0, | 0.0, |
| 0.7963, | 0.7963, | 0.333333, |
| 0.0, | 0.2037, | 0.666667. |

(2) Expanded $\alpha$-monoclinic selenium:

| $a$ | $b$ | $c$ |
|---|---|---|
| 9.14955 Å, | 9.16977 Å, | 11.7377 Å. |

Altered atomic coordinates:

| $u$ | $v$ | $w$ |
|---|---|---|
| 0.3175, | 0.480, | 0.2344, |
| 0.4224, | 0.6568, | 0.3531, |
| 0.3136, | 0.6301, | 0.5292, |
| 0.1325, | 0.8111, | 0.5500, |
| 0.9199, | 0.6785, | 0.5153, |
| 0.8457, | 0.7250, | 0.3244, |
| 0.9169, | 0.5143, | 0.2265, |
| 0.1296, | 0.5905, | 0.1325. |

(3) Expanded $\beta$-monoclinic selenium:

| $a$ | $b$ | $c$ |
|---|---|---|
| 12.940 Å, | 8.1265 Å, | 9.3752 Å. |

Altered atomic coordinates:

| $u$ | $v$ | $w$ |
|---|---|---|
| 0.5799, | 0.3128, | 0.4340, |
| 0.4737, | 0.2254, | 0.2443, |
| 0.3257, | 0.3952, | 0.2383, |
| 0.3496, | 0.5760, | 0.0497, |
| 0.4072, | 0.8252, | 0.1559, |
| 0.5859, | 0.8342, | 0.1410, |
| 0.6554, | 0.7488, | 0.3654, |
| 0.7051, | 0.4757, | 0.3318. |

## APPENDIX B: DEFINITIONS OF THERMAL AND STATIC DISPLACEMENT

$\sigma_\infty^2$ is the mean-square deviation of the distance of separation between two atoms whose individual displacements are mutually independent.

$\sigma_i^2$ is the mean-square deviation of the distance between two atoms whose separation is $r_i$, the radius of the $i$th shell of neighbors in a crystalline structure.

$\gamma_i$ is the $i$th coupling factor. $\gamma_i=\sigma_i^2/\sigma_\infty^2$.

$\langle u_s^2\rangle_{\text{av}}$ is the mean-square deviation, along direction $\mathbf{s}$, of the position of an atom from its mean position.

$\langle u_{\text{thermal}}^2\rangle_{\text{av}}$ is the mean-square deviation in three dimensions of the position of an atom from its mean position due to thermal vibrations.

$\langle u_s^2\rangle_{\text{av}}$ is the component of the mean-square deviation of the position of an atom from its mean position along any one (unspecified) direction. If the displacements are isotropic, $\langle u^2\rangle_{\text{av}}=3\langle u_s^2\rangle_{\text{av}}=\frac{3}{2}\sigma_\infty^2$.

$\langle u_{\text{static}}^2\rangle_{\text{av}}$ is the mean-square three-dimensional deviation of the mean position of an atom from an ideal position.

$\langle u_{\text{total}}^2\rangle_{\text{av}}$ is the mean-square three-dimensional deviation of the position of an atom from an ideal position. For most reasonable distributions of displacements, $\langle u_{\text{total}}^2\rangle_{\text{av}}=\langle u_{\text{thermal}}^2\rangle_{\text{av}}+\langle u_{\text{static}}^2\rangle_{\text{av}}$.